



Study of paramagnetic defect centers in as-grown and annealed TiO₂ anatase and rutile nanoparticles by a variable-temperature X-band and high-frequency (236 GHz) EPR

S.K. Misra ^a, S.I. Andronenko ^{a,1}, D. Tipikin ^b, J.H. Freed ^b, V. Somani ^c, Om Prakash ^c

^a Physics Department, Concordia University, 1455 de Maisonneuve Blvd West, Montreal, QC, Canada H3G 1M8

^b ACERT Biomedical Center, Baker Laboratory, Cornell University, Ithaca, NY 14853-1301, USA

^c Department of Metallurgical Engineering and Material Science, Indian Institute of Technology, Powai, Mumbai 400076, India



ARTICLE INFO

Article history:

Received 9 August 2015

Received in revised form

9 September 2015

Accepted 19 October 2015

Available online 20 October 2015

Keywords:

EPR

Nanoparticle

Anatase

Rutile

TiO₂

Fe³⁺ ion

ABSTRACT

Detailed EPR investigations on as-grown and annealed TiO₂ nanoparticles in the anatase and rutile phases were carried out at X-band (9.6 GHz) at 77, 120–300 K and at 236 GHz at 292 K. The analysis of EPR data for as-grown and annealed anatase and rutile samples revealed the presence of several paramagnetic centers: Ti³⁺, O[−], adsorbed oxygen (O₂[−]) and oxygen vacancies. On the other hand, in as-grown rutile samples, there were observed EPR lines due to adsorbed oxygen (O₂[−]) and the Fe³⁺ ions in both Ti⁴⁺ substitutional positions, with and without coupling to an oxygen vacancy in the near neighborhood. Anatase nanoparticles were completely converted to rutile phase when annealed at 1000°C, exhibiting EPR spectra similar to those exhibited by the as-grown rutile nanoparticles. The high-frequency (236 GHz) EPR data on anatase and rutile samples, recorded in the region about g=2.0 exhibit resolved EPR lines, due to O[−] and O₂[−] ions enabling determination of their g-values with higher precision, as well as observation of hyperfine sextets due to Mn²⁺ and Mn⁴⁺ ions in anatase.

© 2015 Elsevier B.V. All rights reserved.

1. Introduction

Nanosize titanium dioxide (TiO₂) exists at room temperature in different phases, namely anatase, rutile and brookite. Pure single crystals of TiO₂ exist only in rutile structural phase. On the other hand, only Fe³⁺, Al³⁺, Mg²⁺ impurities can stabilize anatase and Mg²⁺ impurity stabilizes brookite phase [1,2]. TiO₂ nanoparticles have received considerable attention from material researchers due to its interesting properties and many technical applications. For example, TiO₂ nanoparticles find usage in paint (as pigments) [3], cosmetics [4], dielectrics [5], electrochromics [6], organic pollutant on windows [7], water/air purifier and deodorizer [8], lithium-ion batteries [9], dye-sensitized solar cells [10], gas sensors [11], catalyst supports [12], photocatalysis [13], photo voltaic cells [14], luminescent [15], biomaterials [16]. Such a vast range of applications is possible due to the two commonly occurring polymorphs of TiO₂, rutile and anatase, which are significantly different in their physical and electronic properties [17]. Particle size, besides other parameters, plays an important role in determining the properties of TiO₂. For

example, energy bandgap of bulk anatase is about 3.2 eV, while the 5–10 nm size anatase particle exhibits a band gap which is ~0.1–0.2 eV higher than that of bulk anatase [17]. This bandgap increase gives an advantage to nanosized TiO₂ over the bulk TiO₂ in some specific applications where increased band gap is required, an example being photovoltaic devices. Recently ferromagnetism up to 880 K was found both in thin films of TiO₂ [18] and nanoparticles of TiO₂ [17]. It was found, that saturation magnetization increased with long annealing in vacuum. The ferromagnetism disappears after annealing in oxygen atmosphere, being converted to the paramagnetic state [19]. Several methods of synthesis of TiO₂ nanoparticles have been reported in the literature, e.g., sol-gel [20], hydrothermal [21], citrate-gel [22], hydrolysis [23], or gas-phase pyrolysis of titanium tetrachloride [24], direct oxidation of titanium platelets [25], metal organic chemical vapor deposition (MOCVD) [26].

It is interesting to compare the properties of anatase and rutile nanoparticles, which possess such different surface morphologies. The technique of electron paramagnetic resonance (EPR) is very sensitive to the investigation of defects or paramagnetic centers in oxides, and thus quite capable of revealing such differences. The present paper is devoted to a detailed EPR study of as-grown anatase and rutile samples, as well as those of annealed samples. The

¹ On leave from Institute of Physics, Kazan Federal University, 18 Kremlevskaya Street, Kazan, 420008, Russia.

purpose of this work, among others, is to confirm the conversion from anatase structure to rutile structure by annealing in air atmosphere by EPR. To this end, several samples of anatase, annealed at different temperatures from 700 °C to 1000 °C, were investigated by EPR. In addition, the EPR spectra are exploited to reveal the presence of paramagnetic centers in anatase and rutile phases of TiO₂, namely the presence of O[−] and Ti³⁺ ions in anatase and rutile TiO₂ nanoparticles.

2. Relevant EPR studies

EPR has been widely used in the study of TiO₂ nanoparticles. There have been reported several EPR studies of anatase and rutile TiO₂ polycrystals and nanoparticles [27–40]. They reveal presence of the paramagnetic centers: oxygen ions, O[−], oxygen vacancies, and the titanium ion, Ti³⁺. The following reactions produced oxygen and titanium ions in these samples by IR or X-ray irradiation: O^{2−} + h⁺ = O[−], Ti⁴⁺ + e[−] = Ti³⁺. Usually, the oxygen and titanium ion are observed in anatase and rutile nanoparticles with different relative intensities, depending on the irradiation and annealing in neutral or oxygen atmosphere, as well on the localization on the surface or in the core of nanoparticles. EPR of oxygen ions with trapped hole (O[−]) in single crystals of anatase were investigated by Grunin et al. [27] ($g_x=2.0029$, $g_y=2.0140$, $g_z=2.0265$) and those in rutile by Yang et al. [28] ($g_x=2.0040$, $g_y=2.0129$, $g_z=2.0277$). EPR studies of the titanium ion (Ti³⁺) with trapped electron in single crystal of TiO₂ of anatase were reported by Sekiya et al. [29] ($g_x=1.993$, $g_y=1.993$, $g_z=1.964$) and those in rutile by Chester [30] ($g_x=1.9732$, $g_y=1.9765$, $g_z=1.9405$).

Temperature treatment of irradiated anatase TiO₂ powder by EPR was reported by Nakaoka et al. [31]. They found that photo-produced holes were trapped at the surface in untreated powder, forming Ti⁴⁺O[−]Ti⁴⁺OH[−], while they were trapped on the surface in heated powder, forming Ti⁴⁺O^{2−}Ti⁴⁺O[−]. Photoproduced electrons trapped Ti³⁺ at the surface of unheated powder, while they trapped Ti³⁺ at the inner part of heat-treated powder. Effect of crystal size on the surface defects of anatase nanoparticles was reported by Kongsuebchart et al. [32]. They showed that the ratios of surface defect/specific surface area increased with increasing TiO₂ crystal size, which led to higher photocatalytic activity. Enhancement of catalyst activity of rutile and rutile/anatase composition was investigated by Canevali et al. [33]. They found that the EPR spectra recorded under UV irradiation show enhanced charge separation in sol-gel samples, showing higher amount of O[−] species after irradiation. Illumination of TiO₂ anatase and rutile powder at 4.2 K resulted in the detection of electrons being trapped at Ti⁴⁺ sites within the bulk, and the holes being trapped at lattice oxide ions at the surface [34]. Xiong et al. [35] investigated dynamics of Ti³⁺ ions on the surface of TiO₂ nanoparticles. Chiese et al. [36] studied electron localization in the process of trapping in TiO₂ nanoparticles. The problem of localization of electron spin density was tackled by means of pulse-EPR hyperfine techniques on samples enriched with ¹⁷O. This approach led to the evidence of a substantial difference in terms of wavefunction localization between anatase (electrons trapped at regular lattice sites exhibiting delocalized electron density) and rutile (interstitial sites showing localized electron density). Macdonald et al. [37] also investigated trapping in TiO₂ nanoparticles. They found that irradiation in vacuum, in the absence of reactants, produced weak EPR signals of O[−] and Ti³⁺ ions. Sun et al. [38] investigated EPR spectra of F-centers (oxygen vacancy with trapped electron) in nanoparticles of anatase, finding an EPR signal at $g=2.0034$. Their results showed, that the kinetics of F-centers is dominated by surface processes, rather than by bulk processes. Coronado et al. [39]

investigated surface characteristics of irradiated nanostructured TiO₂. They found that the behavior of the samples, as prepared by hydrothermal (H) and thermal (T) treatments are different under UV irradiation. They found that the samples of H series after irradiation show some Ti³⁺ centers, while only weak signals associated with oxygenated radicals were observed for T samples, because these radicals are thermally unstable. Komagichi et al. [40] investigated electron transfer from anatase to rutile in reduced TiO₂ nanoparticles, finding that trapped electrons can be transferred from anatase phase to rutile phase by photoexcitation. EPR spectra of the Fe³⁺ ion in single crystals of rutile and anatase have been reported [41–44]. On the other hand, EPR spectra of the Fe³⁺ ion in polycrystalline TiO₂ were investigated [45,46], and low-field EPR signals were observed. Such signals have also been detected in rutile colloid particles [47]. Several investigations of colloidal anatase [48] and TiO₂ nanoparticles have been reported [49–52]. Annealing of TiO₂ nanoparticles in air leads to the formation of paramagnetic centers, mainly oxygen vacancies [31,35].

3. Structure of rutile and anatase

Both anatase and rutile have tetragonal crystal structures, but they belong to different space groups. Anatase possesses the space group I4₁/amd structure [53] with four formula units in the unit cell, whereas rutile possesses the space group P4₂/mnm [53] structure with two TiO₂ formula units in one unit cell [54,55]. The low-density solid phases of anatase are less stable and undergo transition to rutile in the solid state. The transformation is accelerated by annealing and occurs at temperatures between 450 and 1200 °C [56]. It is dependent upon several parameters, such as initial particle size, initial phase, dopant concentration, reaction atmosphere and annealing temperature [57,58]. The conversion from anatase structure to rutile structure when annealing at atmosphere pressure starts at 600 °C and becomes completed at 1000 °C [59]. The titanium and oxygen atoms are more tightly packed in rutile structure. Anatase and rutile structures can be described in terms of chains of TiO₂ octahedra. In rutile structure, each Ti⁴⁺ ion is surrounded by an octahedron of six O^{2−} ions. The octahedron in rutile is not regular, showing a slight orthorhombic distortion. The octahedron in anatase is significantly distorted so that its symmetry is lower than orthorhombic. The Ti-Ti distance in anatase is greater whereas the Ti-O distances are shorter than in rutile. In the rutile structures each octahedron is in contact with 10 neighbor octahedrons (two sharing edge oxygen pairs and eight sharing corner oxygen atoms), whereas in the anatase structure each octahedron is in contact with eight neighbors (four sharing an edge and four sharing a corner). These differences in lattice structures cause different mass densities and electronic band structures for the two forms of TiO₂. Anatase can be conceived as an arrangement of parallel octahedra, while in the case of rutile some octahedra are rotated by 90°. During conversion from anatase to rutile there occurs a symmetry change from I4₁/amd to P4₂/mnm space group in terms of reconstructive polymorphism. As a consequence, the ionic mobility that occurs during phase transition results in increased densification and coarsening of TiO₂ nanoparticles.

In anatase the Ti⁴⁺ ion is surrounded by six octahedrally coordinated oxygen ions with the point symmetry D_{2d} [27]. The oxygen octahedra are distorted with two long Ti-O bonds and four shorter bonds. In rutile phase the point symmetry for the Ti⁴⁺ ion is D_{2h} [60]. The symmetry of the normal O site is C_{2v}, both in rutile and anatase structures [27,61].

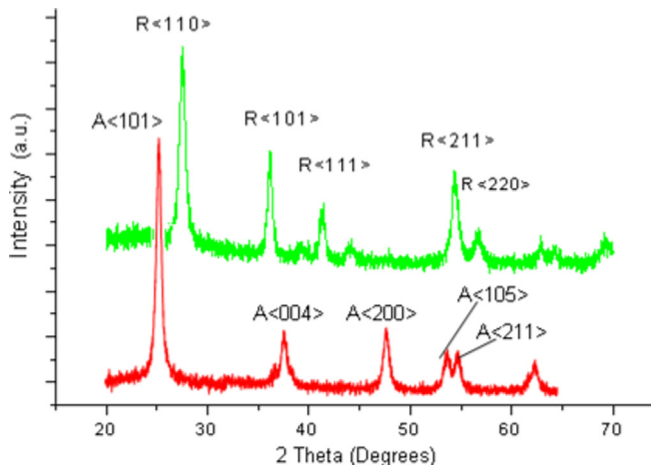


Fig. 1. X-ray diffraction (XRD) patterns of TiO_2 nanopowder samples in rutile and anatase phases. The peaks positions and linewidths show well crystallized anatase (A) and rutile (R) phases with crystallite (Scherrer) size~15 nm.

4. Synthesis and characterization of rutile and anatase nanopowders

In the present work, titania (TiO_2) nanoparticles, both in anatase and rutile phases, were synthesized in small amounts (~1–2 g) by the hydrolysis of titanium tetrachloride, which contained trace amount of Fe^{3+} whose EPR spectrum was detected. **(i) Rutile.** TiO_2 nanopowder, as obtained from acidic (~0.5 pH) suspension, aged for about 24 h dried and annealed at 400 °C for 30 min, showed well crystallized rutile peaks in its XRD pattern as shown in Fig. 1. **(ii) Anatase.** TiO_2 nanopowder, obtained from the ~8 pH -treated suspension, low temperature dried and annealed at 400 °C for 30 min, showed clean XRD peaks due only to the anatase TiO_2 phase. Phase and crystallinity of the fine powders of rutile and anatase were checked by examining their X-ray diffraction patterns by the use of an Xpert pro-model and Cu K_{α} radiation. It is noted that good photocatalytic performance is obtained with heat-treated titanium dioxide at temperatures between 450 °C and 600 °C where EPR spectra of complexes of the

trivalent titanium ions and other localized magnetic centers often coexist. The content of these localized magnetic centers significantly affects their physical properties, which play an appropriate role in their applications.

The TEM images of rutile and anatase powders, respectively, are shown in Fig. 2(A) and (B). They reveal that TiO_2 particles are more or less spherically shaped with the particle size being between 10 and 15 nm, which corroborates with the Scherrer sizes, obtained from X-ray diffraction patterns. The rutile particles are seen to have aggregated in a particular manner, forming rod-like clusters. These rods appears to be coming together to form flower, or leafy bunch, like groups, thereby suggesting self-assembly. On the other hand, the nearly spherical anatase particles appear to have aggregated randomly.

Annealing. Anatase nanoparticles were annealed in air atmosphere at 700 °C, 800 °C, 900 °C, and 1000 °C for 30 min. On the other hand, rutile nanoparticles were also annealed at 900 °C in air and nitrogen gas atmospheres for one hour to ensure removal of any anatase component.

5. Experimental

5.1. Spectrometers

The EPR spectra were recorded using an X-band Bruker ER 200D – SRC spectrometer at Concordia University, and a high-frequency 236.64 GHz EPR spectrometer at ACERT EPR center, Cornell University, Ithaca, New York, USA. The measurements were carried out in the temperature range 77, 110–300 K at X-band using a variable temperature Bruker accessory for low-temperature measurements. At 236.64 GHz the magnetic field was swept only in the region about $g=2.00$, that is in the range of magnetic field from 8.36 to 8.54 T, to obtain a better resolution of EPR lines at about $g=2.00$. This was further enhanced by using several sweeps, up to 150, to increase the intensity of very weak EPR signals, as listed in Table 1.

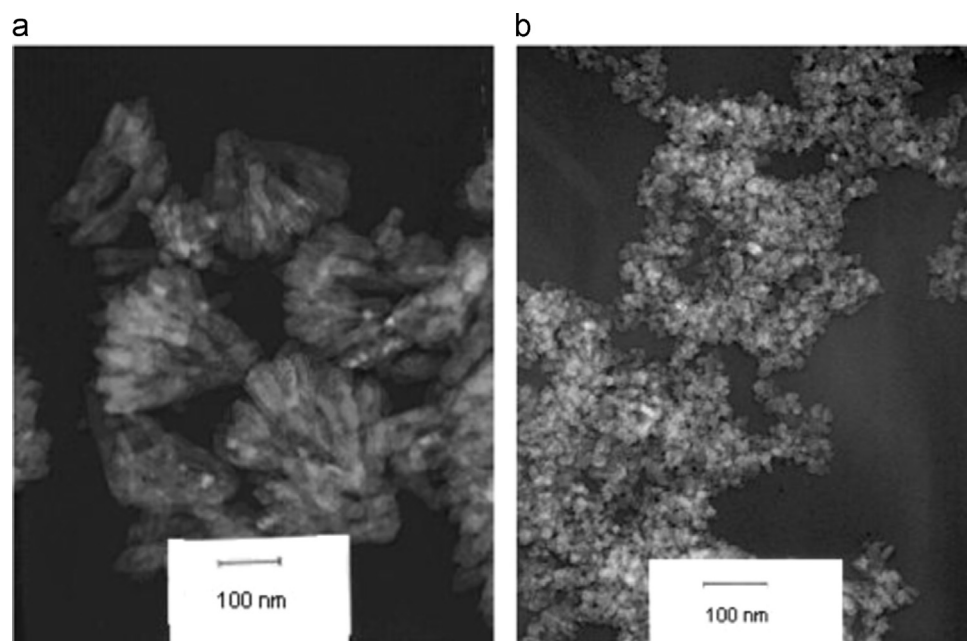


Fig. 2. Transmission electron microscope (TEM) images of (A) rutile, and (B) anatase TiO_2 nanoparticles. The average particle size in both phases is ~15 nm, and the morphology is nearly spherical. The rutile nanocrystallites form bunchy-leaves-like self-assembly pattern (A).

Table 1

A list of the various paramagnetic centers observed in anatase and rutile nanoparticles. (The corresponding g-values for these centers are listed in the captions to Figs. 8, 10–12). Here O^- – ionized oxygen ion, Ti^{3+} – titanium ion, O_2^- – ionized adsorbed oxygen, F center – oxygen vacancy with trapped electron. The number of scans to record EPR spectra at 236 GHz is also listed. (The annealed samples are annealed in air, unless otherwise stated.)

Sample	295 K (9.6 GHz)	77 K (9.4 GHz)	292 K (236 GHz) (8.36–8.54 T)
Anatase			
As-grown annealed at 400 °C	O^- , O_2^- , Ti^{3+} , F center	O^- , O_2^- , Ti^{3+} , F center	F center, 9 scans
Annealed at 700 °C (30 min)	No EPR signal	No EPR signal	F center (weak signal) 31 scans
Annealed 800 °C (30 min)	F center, O_2^- (weak signals)	F center, O_2^-	F center, Mn^{2+} 20 scans
Annealed at 900 °C (30 min)	F center, (weak signals)	F center	F center, Mn^{2+} , Mn^{4+} 50 scan
Annealed at 1000 °C (30 min)	No EPR signal	O^- , O_2^- , Ti^{3+} , F center (weak signals)	O^- , Ti^{3+} , F center (weak signals) 110 scans
Rutile			
As-grown annealed at 400 °C	Fe^{3+} (substitutional), Fe^{3+} (substitutional, with oxygen vacancy in vicinity), O_2^-	Fe^{3+} (substitutional), Fe^{3+} (substitutional, with oxygen vacancy in vicinity), O_2^-	O^- , Ti^{3+} , F center, Mn^{4+} 124 scans (8.14–8.54 T)
Annealed at 800 °C	No data	No data	O^- , Ti^{3+} , F center 150 scans
Annealed at 900 °C, 60 min	Fe^{3+} (substitutional), Fe^{3+} (substitutional, with oxygen vacancy in vicinity), O_2^- (weak signals)	Fe^{3+} (substitutional), Fe^{3+} (substitutional, with oxygen vacancy in vicinity), O_2^-	No data
Annealed at 900 °C, nitrogen gas, 60 min	No EPR signal	No EPR signal	No data

5.2. EPR spectra

Table 1 lists the various EPR signals observed in anatase and rutile samples. Fig. 3 exhibits the temperature dependence of X-band EPR spectra of as-as-grown anatase nanoparticles. Fig. 4 shows 236-GHz EPR spectra of as-grown anatase samples at 292 K. Fig. 5a–c show the X-band EPR spectra of the anatase sample annealed at 1000 °C at 295 K, 77 K and the central part ($g\sim 2.00$) of the spectrum at 77 K, respectively. Fig. 6a–d show the 236-GHz EPR spectra at 292 K of anatase samples annealed at 700 °C, 800 °C, 900 °C, and 1000 °C, respectively. Fig. 7 exhibits the temperature dependence of the X-band EPR spectrum of as-grown rutile nanoparticles. Fig. 8 shows the 236-GHz EPR spectra of as-grown rutile sample at 292 K; the inset to Fig. 8 shows the corresponding X-band spectrum. Fig. 9a and b, respectively, exhibit at 295 K and at 77 K the X-band EPR spectra of rutile nanoparticles annealed at 900 °C in air and in nitrogen atmospheres. Fig. 10

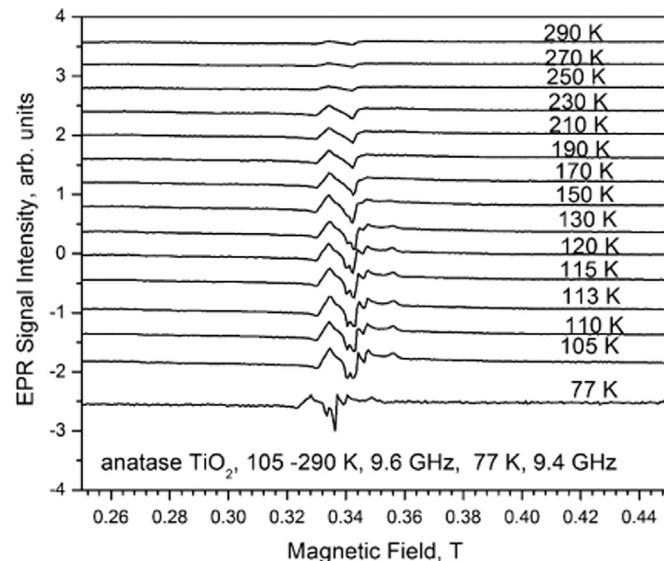


Fig. 3. X-band (9.6 GHz) EPR spectra of as-grown anatase TiO_2 nanoparticles at various temperatures in the range 105–290 K. N.B. The spectrum at 77 K is at 9.4 GHz, and therefore the corresponding lines appears slightly shifted to lower fields.

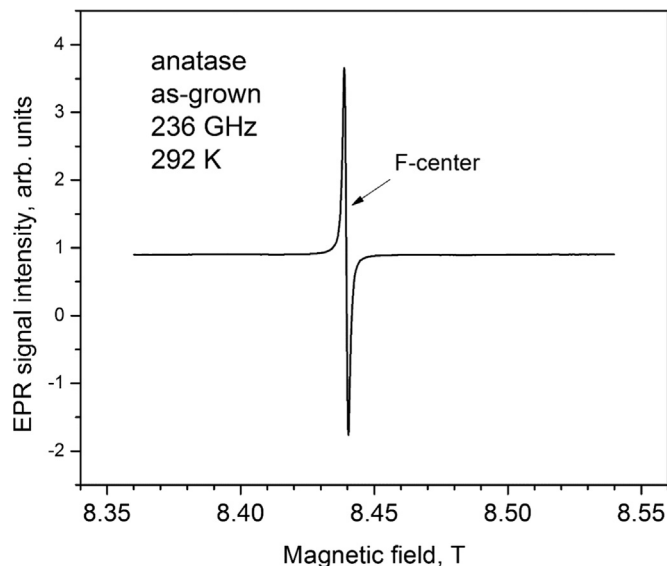


Fig. 4. The central part ($g\sim 2.0$) of 236-GHz EPR spectrum of as-grown anatase TiO_2 nanoparticles at 292 K due to the F-center ($g=2.003$).

shows the experimental and simulated EPR spectra of rutile sample, annealed at 800 °C. Fig. 11 a–c, respectively, show experimental and simulated X-band EPR spectra of as-grown rutile samples at 77 K, 77 K (central line spread over 0.30–0.38 T) and at 295 K. Fig. 12 a and b show experimental and simulated X-band EPR spectra of as-grown anatase samples at 77 K (0.32–0.36 T), and 295 K, respectively.

5.3. Anatase

5.3.1. As-grown samples

(a) X-band (77, 110–290 K): As shown in Fig. 3, at 290 K two main EPR lines were observed, situated at 332 mT and 343.5 mT, due to adsorbed oxygen (O_2^-) and the Ti^{3+} ion and O^- ion, respectively, as confirmed by simulation (Section 5.3). They became narrower and split with decreasing temperature. Finally, at 77 K several EPR signals situated at 325.4, 333.8, 335.7, 340, 347.9 were observed. **(b) 236 GHz (292 K):** The EPR spectra were recorded from 8.36 to 8.54 T and are shown in Fig. 4. Only one EPR line at

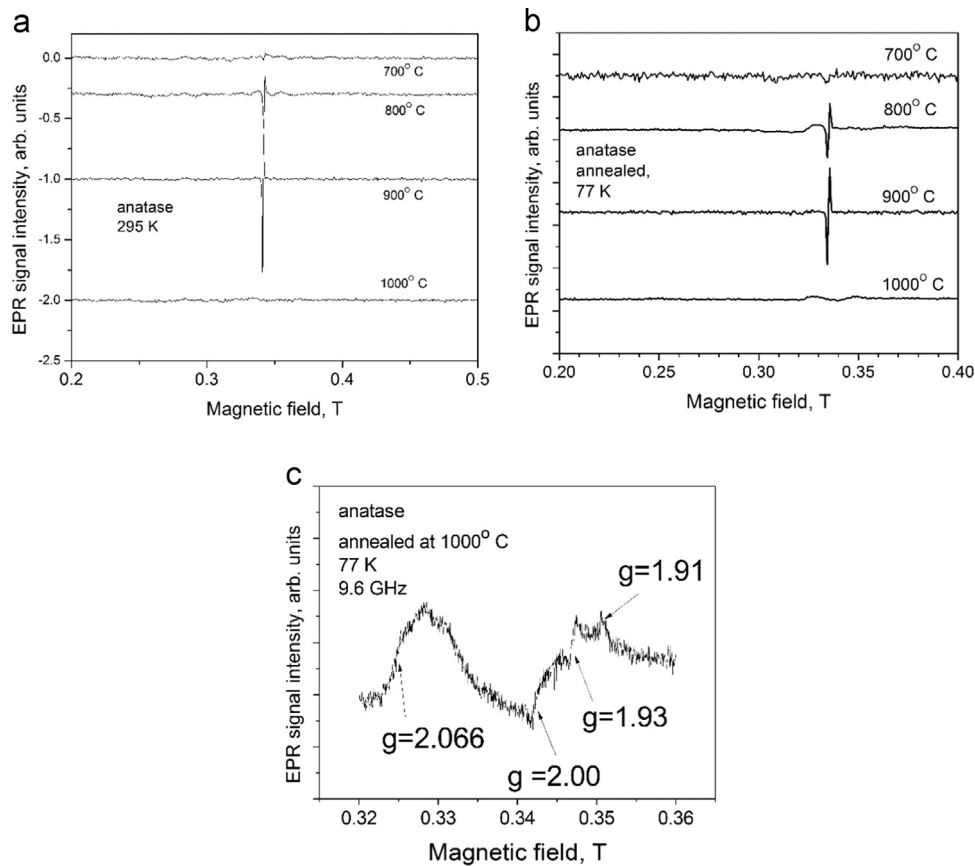


Fig. 5. X-band EPR spectra of anatase TiO₂ nanoparticles annealed at 700, 800, 900, 1000 °C at (a) 295 and (b) 77 K. The central part of the EPR spectrum of anatase sample annealed at 1000 °C is shown in Fig. 5(c).

8.44 T, due to an electron trapped by oxygen vacancy (F-center), was observed in this sample in the magnetic field range investigated. It is much narrower than that at X-band, presumably due to line narrowing at high frequency (10/3: exchange narrowing) [62].

5.3.2. Annealed samples

(a) **X-band (77 K):** Fig. 5a and b show the EPR spectra for anatase samples annealed at 700 °C, 800 °C, 900 °C, 1000 °C at 295 and 77 K, respectively; a magnified view of the central part of the spectrum of the sample annealed at 1000 °C at 77 K is shown in Fig. 5c. It is seen from Fig. 5b that there is a semblance of only a very weak signal located at 335 mT in the anatase sample annealed at 700 °C. The intensity of this signal gradually increases in samples with increasing annealing temperature at 800 and 900 °C. The EPR spectrum in the sample annealed at 1000 °C is different from those annealed at lower temperatures; only two very weak, broad lines centered at 324.5 mT and 345.2 mT (average) appeared at 77 K. The latter EPR line consists of three narrow EPR lines, at 342.2, 345.0, and 350.0 as shown in Fig. 5c. (b) **236 GHz (292 K):** The EPR spectra for anatase samples annealed at 700 °C, 800 °C, 900 °C, 1000 °C, recorded from 8.36 to 8.54 T, are shown in Figs. 6 a-d, respectively. As seen from Fig. 6a, there appears only one unsplit EPR signal, 8.44 T. However, in Fig. 6b and c for the samples annealed at 800 °C and 900 °C, respectively, this signal appears split, which is due to the appearance of hyperfine (hf) central sextet of the Mn²⁺ ion (8.452 T with the hf constant $A=8.0$ mT), where one of the hf lines overlap the line at 8.440 T. On the other hand, in the EPR spectrum of the sample annealed at 900 °C, one sees another hf central sextet due to the Mn⁴⁺ ion (8.502 T, with hf constant $A=7.5$ mT) not observed for the sample annealed at

800 °C. The intensity of the Mn²⁺ sextet relative to that of the Mn⁴⁺ sextet becomes smaller, which is due to its oxidization (increasing valence of Mn ion to Mn⁴⁺) in air atmosphere. As for the hyperfine sextets, it is noted that Mn⁴⁺ ions substitute for Ti⁴⁺ ions in TiO₂, whereas Mn²⁺ ions are present as impurity in interstitial positions. For the sample annealed at 1000 °C, none of the hf sextets due to Mn²⁺ and Mn⁴⁺ ions are observed as seen in Fig. 6d. The intensity of the EPR signal at 8.44 T increases with increasing annealing temperature of the samples. This is because more oxygen vacancies are created with increasing annealing temperature, contributing to the intensity of this signal, which is due to an electron trapped by an oxygen vacancy (F-center) [38]. In the anatase samples annealed at 1000 °C the EPR line at 8.440 decreases significantly in intensity, as shown in Fig. 6d. In addition, in this sample a new EPR line appears, situated at 8.525 T, due to Ti³⁺ ions, as confirmed by simulation (Section 5.4, Fig. 8) similar to that observed in as-grown rutile sample at 236 GHz, shown in Fig. 8, indicating that the sample has almost completely converted to rutile after annealing at 1000 °C.

5.4. Rutile

5.4.1. As-grown samples

(a) **X-band (77, 110–295 K):** As shown in Fig. 7, at room temperature the EPR spectrum consists mainly of three EPR lines situated at 332 mT (most intense), at 314 mT, and at 308 mT, as shown in more detail in the inset in Fig. 8, as well as of weak lines at low magnetic fields at 80, 120, 160, 200, 260 mT ($g=8.3, 5.7, 4.3, 3.3, 2.6$). These weak lines increase in intensity as the temperature decreases, becoming comparable to that of the central line at 332 mT at temperatures ≤ 190 K. (b) **236 GHz (292 K):** An EPR spectrum was

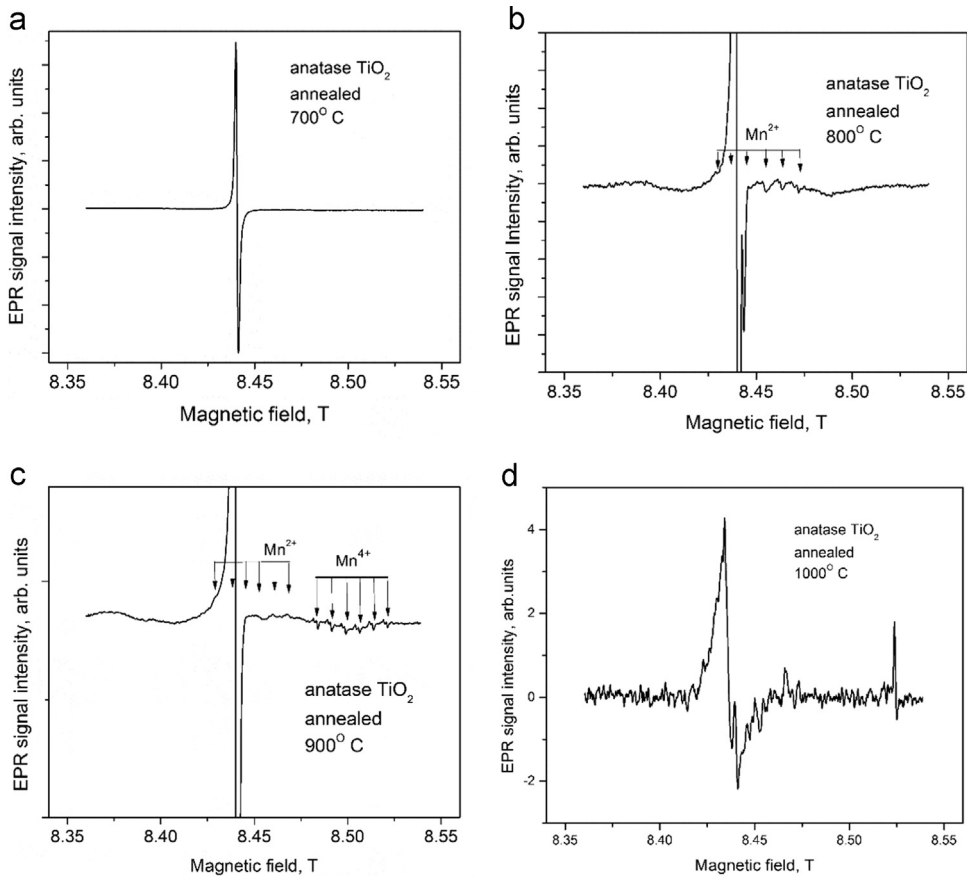


Fig. 6. The central part (8.35–8.55) of the 236-GHz EPR spectrum at 292 K of anatase TiO₂ nanoparticles annealed at (a) 700, (b) 800, (c) 900, (d) 1000 °C. The central hyperfine sextets of Mn²⁺ (8.452 T) and Mn⁴⁺ (8.502 T) are clearly observed for the sample annealed at 900 °C, as shown in Fig. c. The sharp line at 8.440 T in the four spectra is due to the F-center.

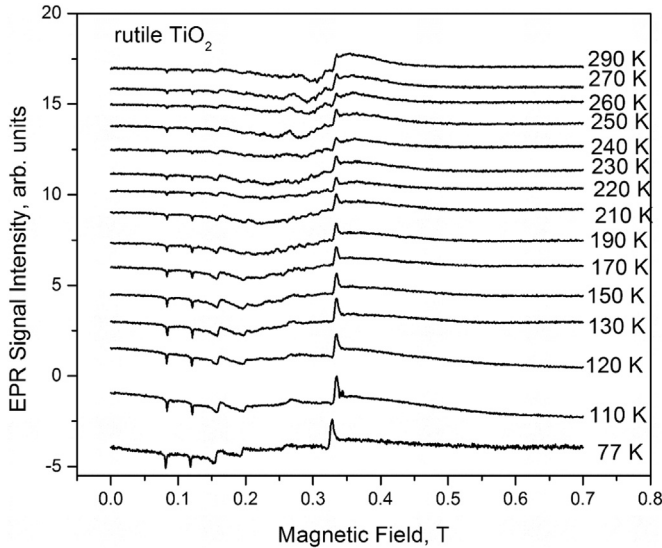


Fig. 7. X-band (9.6 GHz) EPR spectra of as-grown rutile TiO₂ nanoparticles at various temperatures in the range 110–290 K. The spectrum at 77 K is at recorded at 9.4 GHz, so that the corresponding lines appears slightly shifted to lower fields relative to those at higher temperatures.

observed in the magnetic field range 8.14–8.54 T, consisting of four EPR lines at 8.275, 8.346, 8.440 and 8.524 T, as shown in Fig. 8. In addition, a hyperfine sextet of EPR lines, characterized by $g=1.997$ and hyperfine constant $A=8.0$ mT, was observed due to the Mn²⁺ ion, similar to that reported in rutile sample doped with Mn [45].

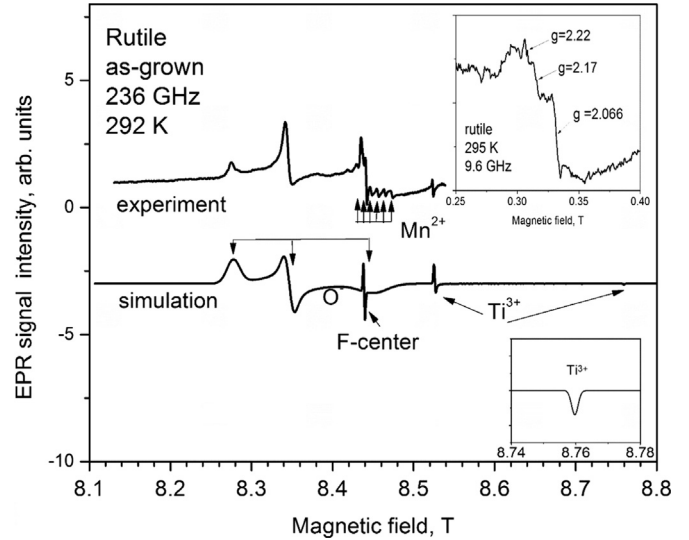


Fig. 8. The experimental and simulated central part (8.1–8.6 T) of 236-GHz EPR spectrum of as-grown rutile TiO₂ nanoparticles at 292 K. The inset shows the corresponding central part of the EPR spectrum at 9.6 GHz at 295 K. The simulations of 236-GHz EPR spectrum was made using the following SH parameters – O[–]: $g_x=2.00$, $g_y=2.025$, $g_z=2.042$, $\Delta B_x=15$ mT, $\Delta B_y=5$ mT, $\Delta B_z=7$ mT; Ti³⁺: $g_x=g_y=1.983$ (the simulated line at 8.76 T for Ti³⁺ at $g_z=1.930$ is beyond the experimental range investigated, shown in the inset with magnification), $\Delta B_x=\Delta B_y=\Delta B_z=1$ mT; F-center: $g_x=g_y=g_z=2.003$, $\Delta B_x=\Delta B_y=\Delta B_z=1$ mT.

5.4.2. Annealed samples: X-band

(a) (900 °C, 77, 295 K). The EPR spectra of the samples annealed

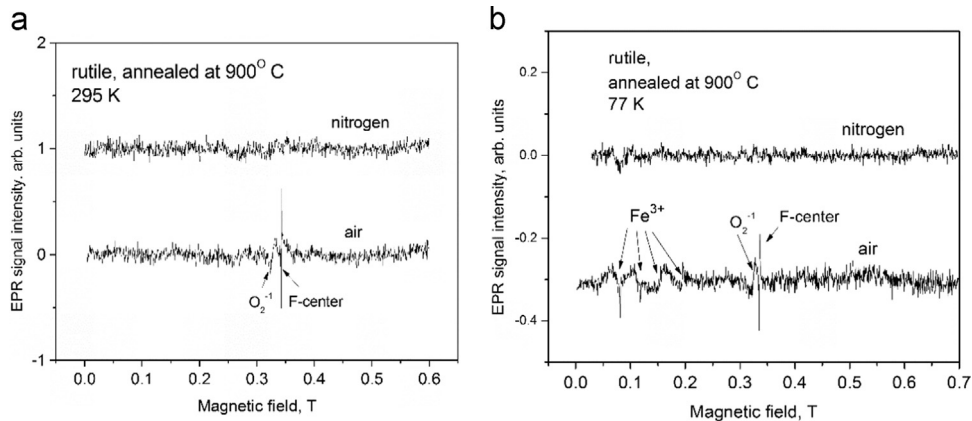


Fig. 9. X-band EPR spectra of rutile nanoparticles, annealed at 900 °C, in air and in nitrogen atmospheres: (a) at 295 and (b) at 77 K. The lines are identified by comparing with the corresponding EPR in as-grown rutile samples.

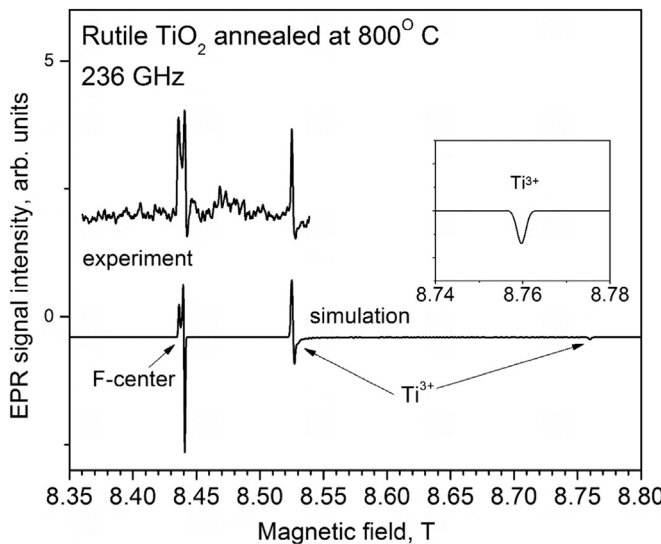


Fig. 10. The central part ($g \sim 2.0$) of 236-GHz EPR spectrum of rutile nanoparticles annealed at 800 °C at 292 K. The simulation is done using the following SH parameters – F-center: $g_x = g_y = 2.003$, $g_z = 2.004$, $\Delta B_x = \Delta B_y = \Delta B_z = 1.0$; Ti^{3+} : $g_x = 1.983$, $g_y = 1.983$, $g_z = 1.930$, $\Delta B_x = \Delta B_y = \Delta B_z = 1.8$ mT; the simulated line for Ti^{3+} at $g = 1.930$ is beyond the experimental range investigated, shown here in the inset with magnification. These g -values are consistent with those used for the simulation at X-band (Fig. 12).

at 900 °C in air and nitrogen gas are different from each other as shown in Fig. 9a and b at 295 K and 77 K, respectively. The very narrow EPR line observed at 335 mT is due to F-center and the broad line at 324 mT at 77 K is due to adsorbed oxygen (O_2^{-1}) in the sample annealed in air. These lines are not present at both 77 K and 295 K in the sample annealed in nitrogen. The low-field EPR lines, observed in the range 50–200 mT, due to the Fe^{3+} ion, as simulated in Section 5.3 are observed in both the samples at 77 K. **(b) 236 GHz (800 °C, 292 K):** The EPR spectrum of the sample annealed at 800 °C is shown in Fig. 10, which also includes the simulated spectrum as described in Section 6. Two EPR signals were observed, located at 8.440 T and 8.525 T, similar to those observed in as-grown rutile sample, as shown in Fig. 8, except for the hyperfine sextet. The split line at 8.44 T in Fig. 10 is due to an oxygen vacancy with trapped electron (F-center), showing the increased resolution of this line (with anisotropic g -value) at the high frequency of 236 GHz. It was shown by the use of density functional approach that the F-centers with anisotropic g -values ($g_x = g_y = 2.003$ and $g_z = 2.004$) belong to the surface of nanoparticle, while F-centers with isotropic g -values ($g = 2.003$) belong

to a core of nanoparticle [63]. The split line at 8.44 T in Fig. 10 is due to an oxygen vacancy with trapped electron (F-center), showing the increased resolution of this line (with anisotropic g -value) at the high frequency of 236 GHz [63]. The EPR line at 8.524 T is similar to that for as-grown rutile (Fig. 8) due to the Ti^{3+} ion. (The higher resolution at 236 GHz made it possible to observe very weak Ti^{3+} lines, not observed at X-band).

5.5. Simulations of EPR spectra

Simulations were carried out to reproduce observed spectra for a better understanding, as explained below.

- (i) The following spin Hamiltonian (SH) was used for the simulation of EPR spectra of Ti^{3+} , and oxygen vacancy with trapped electron (F-center), ionized oxygen (O^-), and adsorbed oxygen (O_2^-), all characterized by $S=1/2$ in anatase and rutile:

$$\mathcal{H}_S = \mu_B \mathbf{B} \cdot \mathbf{g} \cdot \mathbf{S} \quad (1)$$

which represents the Zeeman interaction, with \mathbf{B} , \mathbf{g} and μ_B being the magnetic-field intensity, g -matrix and the Bohr magneton, respectively. The spectra, so simulated, are shown in Figs. 10 (O^- and Ti^{3+}), 11a–c (O_2^-) and 12 (O_2^- , O^- and Ti^{3+}), for annealed rutile, as-grown rutile, and as-grown anatase samples, respectively. The SH parameters used for simulations are listed in the respective, where the g_i ($i=x,y,z$) are diagonal components of the g -matrix and ΔB_i are the EPR linewidths.

- (ii) The following spin Hamiltonian was used for simulation of the EPR spectrum of Fe^{3+} ($S=5/2$), appropriate to four-fold symmetry consistent with tetragonal structure in rutile [27, 53, 61]:

$$\mathcal{H}_S = \mu_B [g_{\parallel} S_z B_z + g_{\perp} (S_x B_x + S_y B_y)] + \sum_{n=2,4}^{m=0,4} B_n^m O_n^m \quad (m \leq n) \quad (2)$$

In Eq. (2), g_{\parallel} , g_{\perp} are the g -values parallel and perpendicular to magnetic Z-axis; \mathbf{S} ($=5/2$) is the electron spin operator; B_n^m are the spin-Hamiltonian parameters and O_n^m are Stevens operators ($3B_2^0 = D$, $B_2^2 = E$); $n=2,4$, m ($\leq n$) = 0, 2, 4 [64]. The spectra, so simulated, are shown in Fig. 11a, with the SH parameters being listed in Table 2. The Fe^{3+} EPR spectrum consisting of the lines situated at 80, 120, 200, 260 mT, observed in rutile nanoparticle (Figs. 7 and 11) at low magnetic-field values, were simulated using the initial SH parameters for the Fe^{3+} ions substituting for the Ti^{4+} ion in rutile, as reported in [41], using an approach to that used for simulation of Fe^{3+} EPR spectra in SnO_2 nanoparticles at

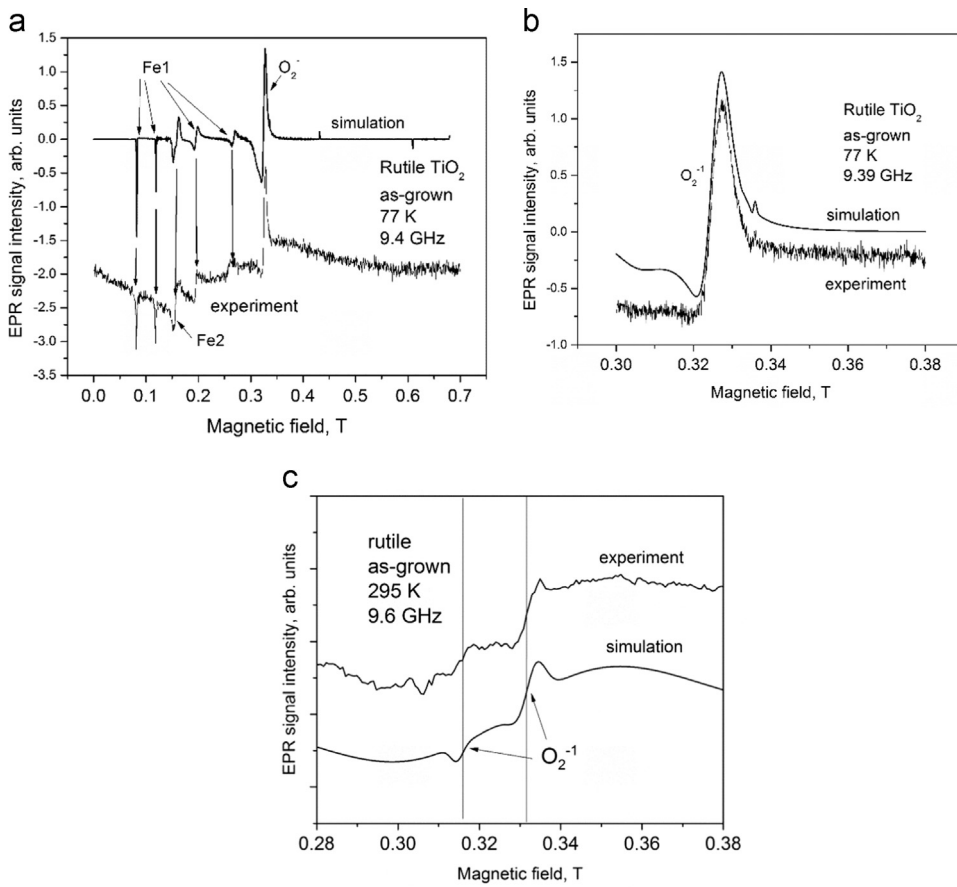


Fig. 11. The experimental and simulated EPR spectra of as-grown rutile sample at 9.4 GHz. **Fig. 11a** shows the EPR lines due to (i) the Fe³⁺ ion in substitutional position (Fe1: $S=5/2$, 4 lines), (ii) the Fe³⁺ ion in substitutional position coupled to an oxygen vacancy (Fe2: $S=5/2$, there is seen only one line in the field range investigated due to a rather large zfs), and (iii) adsorbed oxygen O₂⁻ ($S=1/2$), shown in more detail in **Fig. 11b**. The SH parameters used for simulating the lines due to the two types of Fe³⁺ ions in **Fig. 11a** are listed in **Table 2**, whereas those for adsorbed oxygen (O₂⁻) is made using the following SH parameters: O₂⁻ at 77 K: $g_x=2.06$, $g_y=2.06$, $g_z=2.15$, $\Delta B_x=\Delta B_y=5$ mT, $\Delta B_z=10$ mT. **Fig. 11c** shows the EPR spectrum of adsorbed oxygen (O₂⁻) at 295 K; the simulation is made with the following parameters: $g_x=g_y=2.06$, $g_z=2.18$, $\Delta B_x=\Delta B_y=4.6$ mT, $\Delta B_z=6$ mT.

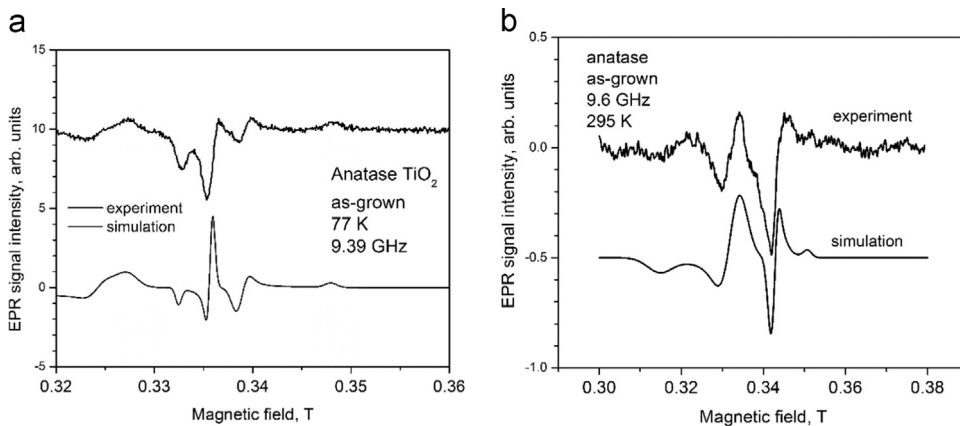


Fig. 12. The experimental and simulated X-band EPR spectra of as-grown anatase TiO₂ nanoparticles at (a) 77 and (b) 295 K. The simulations are done using the following SH parameters: (a) 77 K – Ti³⁺: $g_x=g_y=1.983$, $g_z=1.930$, $\Delta B_x=\Delta B_y=\Delta B_z=2$ mT; O⁻: $g_x=2.00$, $g_y=2.00$, $g_z=2.02$, $\Delta B_x=\Delta B_y=\Delta B_z=1.4$ mT; O₂⁻: $g_x=2.07$, $g_y=2.05$, $g_z=2.17$, $\Delta B_x=\Delta B_y=2$ mT, $\Delta B_z=5$ mT; (b) 295 K – Ti³⁺: $g_x=1.993$, $g_y=1.993$, $g_z=1.955$, $\Delta B_x=\Delta B_y=\Delta B_z=2$ mT; O₂⁻: $g_x=g_y=2.06$, $g_z=2.18$, $\Delta B_x=\Delta B_y=4.6$ mT, $\Delta B_z=6$ mT.

Table 2
Spin Hamiltonian parameters used for the simulation of X-band rutile EPR spectra of the Fe³⁺ ions in Ti⁴⁺ substitutional positions and Ti⁴⁺ substitutional positions coupled to an oxygen vacancy, as shown in **Fig. 11** ($S=5/2$).

Species	$g_x=g_y=g_z$	$D=b_2^0=3B_2^0$ (mT)	B_2^2 (mT)	B_4^0 (mT)	B_4^4 (mT)	$\Delta B_x=\Delta B_y$ (mT)	ΔB_z (mT)
Fe ³⁺ substitutional	2.000	726.1	78.8	2.3	16.3	4	1.6
Fe ³⁺ substitutional (coupled to oxygen vacancy)	2.000	520.0	160.0	–	–	4	4

236 GHz [65,66]. The EPR line at 160 mT in Fig. 11 is due to another Fe^{3+} ion coupled to an oxygen vacancy [42], with the parameters listed in Table 2; only one line is seen due to the rather large values of the zero-field splitting parameters

5.6. Analysis of observed EPR spectra

Here the assignments of the EPR lines to the various paramagnetic centers are based on the similarity of the SH parameters to those reported in the literature.

5.6.1. Anatase

5.6.1.1. As grown. The X-band EPR spectra at 77 K in anatase nanoparticles (Fig. 12) show the presence of (i) O^- ($S=1/2$, $g_x=2.00$, $g_y=2.01$, $g_z=2.03$), (ii) adsorbed oxygen O_2^- ($S=1/2$, $g=2.07$), (iii) oxygen vacancy with trapped electron (F-center) ($S=1/2$, $g=2.003$, narrow EPR line), (iv) Ti^{3+} ion ($S=1/2$, $g_x=1.97$, $g_y=1.97$, $g_z=1.93$). All these EPR signals have been reported previously [31,35,54]. The SH parameters for the Ti^{3+} ion in anatase nanoparticle are closer to their values in TiO_2 anatase single crystal [29] at 295 K, but those at 77 K are closer to their values in rutile crystals [30].

5.6.1.2. Annealed. The strong EPR signal at $g=2.003$ in the samples annealed in air at 800 °C, 900 °C is due to oxygen vacancy with trapped electron [38,67]. It was not observed in the sample annealed at 1000 °C.

5.6.2. Rutile

5.6.2.1. As grown. The X-band EPR spectra due to the Fe^{3+} ion in substitutional position, described by the SH given by Eq. (2), as shown in Fig. 11a, have been widely reported in the literature [45–50], but a simulation was only carried out in the present work to confirm their presence. They are due to the Fe^{3+} ion in Ti^{4+} substitutional position, with (1 line, 160 mT) and without (4 lines) coupling to an oxygen vacancy in nearest vicinity. The EPR line at 160 mT is similar to that observed for charge-compensated Fe^{3+} ion in anatase powder [42]. Only one EPR line, due to adsorbed oxygen (O_2^-), was observed at 77 K at 324.5 mT, as shown in Fig. 11b. The central broad EPR signal at 324.5 mT in Fig. 8 (inset) is due to adsorbed oxygen (O_2^-). At room temperature it consists of three EPR lines at 332 mT (most intense), 314 mT and 308 mT as shown in Fig. 11c. In the EPR spectrum at 236 GHz of as-grown rutile sample, shown in Fig. 8, the EPR lines at 8.275 T, 8.346 T and 8.44 T are due to O^- ion, as confirmed by the simulation with the SH parameters listed in the caption to Fig. 8, whereas the EPR line at 8.525 T is due to the Ti^{3+} ion. These lines are not observed at X-band because of their very low intensity; they become observed at 236 GHz only after several (up to 150) magnetic field sweeps.

5.6.2.2. Annealed.: As seen from Fig. 9a, b the rutile sample annealed at 900 °C in air exhibited EPR signals at 2.003 and 2.066, due to an F-center and adsorbed oxygen (O_2^-), respectively, as discussed in Section 5.2, whereas that annealed in nitrogen atmosphere did not exhibit these lines. The EPR spectrum at 236 GHz of rutile sample annealed at 800 °C (Fig. 10) is similar to that observed in as-grown rutile sample (Fig. 8).

5.6.3. Differences between the EPR spectra of anatase and rutile nanoparticles

Anatase nanoparticles exhibit EPR spectra due to the presence of Ti^{3+} and O^- ions, adsorbed oxygen (O_2^-), F-centers (oxygen vacancy with trapped electron). Annealing anatase samples at 700–900 °C, increases the intensity of the signals due to the F-centers; this signal disappears in the sample, annealed at 1000 °C. The EPR spectra in rutile nanoparticles reveal, in general,

the presence of the same paramagnetic centers as in anatase samples. However, the intensities of the EPR signals due to Ti^{3+} and O^- ions, and F-centers are considerably reduced, as compared to those in anatase samples. Furthermore, the EPR spectra in rutile samples clearly indicate the presence of Fe^{3+} ions in (i) Ti^{4+} substitutional position, and (ii) in Ti^{4+} substitutional positions with oxygen vacancy in nearest vicinity. Annealing rutile samples in air increases the intensity of the EPR signal due to adsorbed oxygen (O_2^-).

5.6.3.1. Transition from anatase to rutile: Usually, when annealing, the transition from anatase to rutile structure begins at 600 °C and becomes completed at 1000 °C [50]. In the present work, the EPR spectrum at 236 GHz in anatase nanoparticles, annealed at 1000 °C, is similar to that in as-grown rutile nanoparticles (see Figs. 8 and 6d), whereas the EPR spectra at 236 GHz of anatase nanoparticles, annealed at 700, 800, 900 °C are similar to those in as-grown anatase nanoparticles (see Fig. 5 and 6a–c). The same transition is found when one compares the EPR spectra in the samples annealed at 900 °C and 1000 °C at X-band (Fig. 5a). This indicates that the transition from anatase to rutile phase occurs for annealing between 900° and 1000 °C. It is noted that the impurities and synthesis conditions (pH of growth solution) can change the conditions of stabilization of anatase and rutile nanoparticles, which may lead to increasing transition temperature.

5.6.3.2. Morphology and surface defects: The above discussion of EPR spectra indicates that rutile structure of TiO_2 , synthesized from acid solution (0.5 pH), is characterized with less defects, than the anatase structure, synthesized from strong (8 pH) acid solution. It can be related to the morphology of rutile and anatase nanoparticles as follows. In rutile nanoparticles, which have aggregated, forming flower, or leafy bunch, like groups, probably all defects have been compensated. On the other hand, anatase nanoparticles aggregated preferably in spherical shape, thus possessing larger free surface, with more surface defects, such as oxygen vacancies.

6. Conclusions

In addition to reviewing published research on EPR in rutile and anatase nanoparticles of TiO_2 , new detailed variable-temperature EPR data have been obtained on the samples prepared here at X-band (~9.5) GHz and at high-frequency (236 GHz); the latter only in the region about $g \approx 2.00$, in order to confirm, among others, the conversion from anatase structure to rutile structure by annealing and to study the formation of various paramagnetic defect centers in anatase and rutile phases of TiO_2 .

The salient features of the X-band and high-frequency EPR investigations made here on as-grown and annealed anatase and rutile TiO_2 nanoparticles are as follows:

- (1) The observed EPR spectra indicate the presence of Ti^{3+} ions, O^- ions, F center (oxygen vacancy with trapped electron), adsorbed oxygen (O_2^-) ions in as-grown anatase and rutile nanoparticles.
- (2) Anatase nanoparticles annealed at 700, 800, 900 °C exhibit increasing intensity of the EPR line due to F center (oxygen vacancy coupled to a trapped electron) with increasing annealing temperature.
- (3) Annealing of anatase nanoparticles at 1000 °C led to complete conversion to the rutile phase.
- (4) The EPR spectra in as-grown rutile TiO_2 nanoparticles revealed the presence of Fe^{3+} impurities, both in the substitutional position and in the substitutional position coupled to an

- oxygen vacancy in the vicinity on the surface of nanoparticles.
- (5) The high frequency measurements at 236 GHz have enabled determination of the anisotropy of the F-center [63] in the rutile sample annealed in air at 800 °C, not possible at X-band.

Acknowledgments.

This research was supported by the Natural Sciences and Engineering Research Council of Canada (NSERC, Grant #A4485 – SKM and SIA) and by the ACERT grant: NIH/NIGMS Grant P41GM103521 (JHF and DT). SA acknowledges partial financial support from Kazan Federal University, Russia.

References

- [1] V.S. Grunin, M.V. Razumeenko, I.B. Patrina, S.K. Filatov, T.V. Alekseyeva, Mode of existence and abundance of TiO_2 -rutile, anatase and brookite, Dokl. Akad. Nauk SSSR, Earth Sci. 268 (3) (1983) 686–688.
- [2] M.V. Razumeenko, V.S. Grunin, A.A. Boitsov, Growth of monocrystals of anatase and brookite by the chemical-transport reaction method, Sov. Phys. Crystallogr. 26 (3) (1981) 371–372.
- [3] C. Feldmann, Preparation of nanoscale pigment particles, Adv. Mater. 13 (17) (2001) 1301–1303.
- [4] V. Rossatto, T. Picatotto, D. Vione, M. Carlotto, Behavior of some rheological modifiers used in cosmetics under photocatalytic conditions, J. Disper. Sci. Technol. 24 (2003) 259–271.
- [5] T. Fuyuki, T. Kobayashi, H. Matsumami, Effects of small amount of water on physical and electrical properties of TiO_2 films deposited by CVD method, J. Electrochem. Soc. 135 (1) (1988) 248–250.
- [6] T. Ohsaku, T. Hirai, An electrochromic display based on titanium dioxide, Electrochim. Acta 27 (9) (1982) 1263–1266.
- [7] I. Sopyan, S. Murasawa, K. Hashimoto, A. Fujishima, Highly efficient TiO_2 film photocatalyst. Degradation of gaseous acetaldehyde, Chem. Lett. 8 (1994) 723–726.
- [8] G.P. Fotou, S. Vemury, S.E. Pratsinis, Synthesis and evaluation of titania powders for photocatalysis of phenol, Chem. Eng. Sci. 49 (24B) (1994) 4939–4948.
- [9] L. Kavan, K. Kratochvílová, M. Gratzel, Study of nanocrystalline TiO_2 (anatase) electrode in the accumulation, J. Electroanal. Chem. 394 (1995) 93–102.
- [10] L. Kavan, T. Stoto, M. Gratzel, D. Fitzmaurice, V. Shklover, Quantum size effects in nanocrystalline semiconducting TiO_2 layers prepared by anodic oxidative hydrolysis of TiCl_3 , J. Phys. Chem. 97 (1993) 9493–9498.
- [11] M. Radecka, M. Rekas, Effect of high temperature treatment on n-p transition in titania, J. Am. Ceram. Soc. 85 (2002) 346–354.
- [12] M. Bankmann, R. Brand, B.H. Engler, J. Ohmer, Forming high surface area TiO_2 to catalyst supports, Catal. Today 14 (2) (1992) 225–242.
- [13] R. Asahi, T. Morikawa, T. Ohwaki, K. Aoki, Y. Taga, Visible-light photocatalysis in nitrogen-doped titanium oxides, Science 293 (5528) (2001) 269–271.
- [14] J. Yamamoto, A. Tan, R. Shiratsuchi, S. Hayase, C.R. Chenthamarakshan, K. Rayeshwar, A 4% efficient dye-sensitized solar cell fabricated from cathodically electrosynthesized composite titania films, Adv. mater. 15 (2003) 1823–1825.
- [15] T. Sekiya, S. Kamei, S. Kurita, Luminescence of anatase TiO_2 single crystals annealed in oxygen atmosphere, J. Lumin. 87–89 (2000) 1140–1142.
- [16] J.M. Wu, H. Satoshi, K. Tsuru, A. Osaka, In vitro bioactivity of anatase film obtained by direct deposition from aqueous titanium tetrafluoride solutions, Thin Solid Films 414 (2002) 275–280.
- [17] K.M. Reddy, S.V. Manorama, A.R. Reddy, Bandgap studies on anatase titanium dioxide nanoparticles, Mater. Chem. Phys. 78 (2002) 239–245.
- [18] S.D. Yoon, Y. Chen, A. Yang, T. Goodrich, X. Zuo, D.A. Arena, K. Ziener, C. Vittoria, V.G. Harris, Oxygen-defect-induced magnetism to 880 K in semiconducting anatase $\text{TiO}_{2-\delta}$ films, J. Phys.: Condens. Matter 18 (2006) L355–L361.
- [19] B. Choudhury, A. Choudhury, Room temperature ferromagnetism in defective TiO_2 nanoparticles: role of surface and grain boundary oxygen vacancies, J. Appl. Phys. 114 (2013) 203906.
- [20] Xiang-huai Xing-zhao Ding, Liu, Synthesis and microstructure control of nanocrystalline titania powders via sol-gel process, Mater. Sci. Eng. A224 (1997) 210–215.
- [21] K. Yu, J. Zhao, Y. Guo, X. Ding, H. Bala, Y. Liu, Z. Wang, Sol-gel synthesis and hydrothermal processing of anatase nanocrystals from titanium n-butoxide, Mater. Lett. 59 (2005) 2515–2518.
- [22] S.R. Dhage, R. Pasricha, V. Ravi, Synthesis of ultrafine TiO_2 by citrate gel method, Mater. Res. Bull. 38 (11–12) (2003) 1623–1628.
- [23] R. Chu, J. Yan, S. Lian, Y. Wang, F. Yan, D. Chen, Shape-controlled synthesis of nanocrystalline titania at low temperature, Sol. State Comm. 130 (12) (2004) 789–792.
- [24] K.Y. Jung, S.B. Park, H.D. Jang, Phase control and photocatalytic properties of nano-sized titania particles by gas-phase pyrolysis of TiCl_4 , Catal. Comm. 5 (2004) 491–497.
- [25] M.K. Akhtar, Y. Xiong, S.E. Pratsinis, Vapor synthesis of titania powder by titanium tetrachloride oxidation, Am. Inst. Chem. Eng. J. 37 (10) (1991) 1561–1570.
- [26] Z. Ding, X. Hu, G.Q. Lu, P.L. Yue, P.F. Greenfield, Novel silica gel supported TiO_2 photocatalyst synthesized by CVD method, Langmuir 16 (15) (2000) 6216–6222.
- [27] V.S. Grunin, G.D. Davtyan, V.A. Ioffe, I.B. Patrina, EPR of Cu^{2+} and radiation centres in anatase (TiO_2), Phys. Status Solidi (b) 77 (1976) 85–92.
- [28] S. Yang, A.T. Brant, L.E. Halliburton, Photoinduced self-trapped hole center in TiO_2 crystals, Phys. Rev. B 82 (2010) 035209.
- [29] T. Sekiya, H. Takeda, N. Kamiya, S. Kurita, T. Kodaira, EPR of anatase titanium dioxide under UV light irradiation, Phys. Status Solidi 3 (10) (2006) 3603–3606.
- [30] P.F. Chester, Electron spin resonance in semiconducting rutile, J. Appl. Phys. 32 (1961) 2233–2236.
- [31] Y. Nakao, Y. Nosaka, ESR investigation into the effects of heat treatment and crystal structure on radicals produced over irradiated TiO_2 powder, J. Photochem. Photobiol. A: Chem. 110 (1997) 299–305.
- [32] W. Kongsuebchart, P. Praserthdam, J. Panpranon, A. Sirisuk, P. Supphasirongjaroen, C. Satayaprasert, Effect of crystalline size on the surface defect of nano- TiO_2 prepared via solvothermal synthesis, J. Cryst. Growth 297 (2006) 234–238.
- [33] C. Canevali, F. Morazzoni, R. Scotti, I.R. Bellobono, M. Giusti, M. Sommariva, M. D'Arienzo, A. Testino, A. Musinu, C. Cannas, Nanocrystalline TiO_2 with enhanced photoinduced charge separation as catalyst for the phenol degradation, Int. J. Photoenergy 2006 (2006) 1–6–90815.
- [34] C.P. Kumar, N.O. Gopal, T.C. Wang, M.-S. Wong, S.C. Ke, EPR investigation of TiO_2 nanoparticles with temperature-dependent properties, J. Phys. Chem. B 110 (2006) 5223–5229.
- [35] Liang-Bin Xiong, Jia-Lin Li, Bo Yang, Ying Yu, Ti^{3+} in the surface of titanium dioxide: generation, properties and photocatalytic application, J. Nanomater. (2012) 831524 (13 p).
- [36] M. Chiesa, M.C. Paganini, S. Livraghi, E. Giannello, Charge trapping in TiO_2 polymorphs as seen by Electron Paramagnetic Resonance spectroscopy, Phys. Chem. Chem. Phys. 15 (2013) 9435–9447.
- [37] I.R. Macdonald, S. Rhydderch, E. Holt, N. Grant, J.M.D. Storey, R.F. Howe, EPR studies of electron and hole trapping in titania photocatalysts, Catal. Today 182 (2012) 39–45.
- [38] Yijun Sun, Takashi Egawa, Chunlin Shao, Liangying Zhang, Xi Yao, Quantitative study of F center in high-surface-area anatase titania nanoparticles prepared by MOCVD, J. Phys. Chem. Solids 75 (2004) 1793–1797.
- [39] J.M. Coronado, A.J. Maira, J.C. Conesa, K.L. Yeung, V. Augugliaro, J. Soria, EPR study of the surface characteristics of nanostructured TiO_2 under UV irradiation, Langmuir 17 (2001) 5368–5374.
- [40] K. Komaguchi, H. Nakato, A. Araki, Y. Harima, Photoinduced electron transfer from anatase to rutile in partially reduced TiO_2 (P-25) nanoparticles: An ESR study, Chem. Phys. Lett. 428 (2006) 338–342.
- [41] D.J. Carter, A. Okaya, Electron paramagnetic resonance of Fe^{3+} in TiO_2 (Rutile), Phys. Rev. 118 (6) (1960) 1485–1490.
- [42] M. Horn, C.F. Schwerdtfeger, EPR of substitutional and charge compensated Fe^{3+} in anatase (TiO_2), J. Phys. Chem. Solids 32 (1971) 2529–2538.
- [43] M. Horn, C.F. Schwerdtfeger, Reinterpretation and temperature dependence of EPR of Fe^{3+} in TiO_2 (anatase), Solid State Commun. 8 (1970) 1741–1743.
- [44] G.J. Lichtenberger, J.R. Addison, E- and X-Band spectroscopy on Fe^{3+} in rutile, Phys. Rev. 184 (1969) 381–382.
- [45] D. Cordischi, M. Valigi, D. Gazzoli, V. Indovina, ESR and reflectance spectra of manganese in polycrystalline TiO_2 (rutile), J. Solid State Chem. 15 (1975) 82–88.
- [46] H.S. Eggleston, J.S. Thorp, EPR spectra of Fe^{3+} and Cr^{3+} in powdered rutile, J. Mater. Sci. 16 (1981) 537–539.
- [47] J. Soria, J.C. Conesa, V. Augugliaro, L. Palmisano, M. Schiavello, A. Sclafani, Dinitrogen photoreduction to ammonia over titanium dioxide powders doped with ferric ions, J. Phys. Chem. 95 (1991) 274–282.
- [48] M. Gratzel, R.F. Howe, Electron paramagnetic resonance studies of doped TiO_2 , Colloids, J. Phys. Chem. 94 (1990) 2566–2572.
- [49] Zhijie Li, Wenzhong Shen, Wensen Hea, Xiaotao Zua, Effect of Fe-doped TiO_2 nanoparticle derived from modified hydrothermal process on the photocatalytic degradation performance on methylene blue, J. Hazard. mater. 155 (2008) 590–594.
- [50] K. Elghniji, A. Atyaoui, S. Livraghi, L. Bousselmi, E. Giannello, M. Ksibi, Synthesis and characterization of Fe^{3+} doped TiO_2 nanoparticles and films and their performance for photocurrent response under UV illumination, J. Alloy. Compd. 541 (2012) 421–427.
- [51] H. Chen, X. Jin, B. Su, Y. Fang, K. Zhu, R. Yang, Preparation of Fe^{3+} -doped TiO_2 nanoparticles and their photocatalytic activities, Ind. J. Chem. 39(A) (2000) 685–689.
- [52] Xinyong Li, Po-Lock Yue, Charles Kotal, Synthesis and photocatalytic oxidation properties of iron doped titanium dioxide nanosemiconductor particles, New. J. Chem. 27 (2003) 1264–1269.
- [53] A.I. Kingon, J.P. Maria, S.K. Streiffer, Alternative dielectrics to silicon dioxide for memory and logic devices, Nature 406 (6799) (2000) 1032–1038.
- [54] W. Li, C. Ni, H. Lin, C.P. Huang, S. Ismat Shah, Size dependence of thermal stability of TiO_2 nanoparticles, J. Appl. Phys. 96 (11) (2004) 6663–6668.
- [55] H. Zhang, J.F. Banfield, New kinetic model for the nanocrystalline anatase-to-rutile transformation revealing rate dependence on number of particles, Am.

- Miner. 84 (4) (1999) 528–535.
- [56] A. Tsevis, N. Spanos, P.G. Koutsoukos, Ab. J. Van der Linde, J. Lyklema, Preparation and characterization of anatase powders, *J. Chem. Soc. Faraday Trans.* 94 (2) (1998) 295–300.
- [57] H.Z. Zhang, J.F. Banfield, Thermodynamical analysis of phase stability of nanocrystalline titania, *J. mater. Chem.* 8 (9) (1998) 2073–2076.
- [58] H.Z. Zhang, J.F. Banfield, Understanding polymorphic phase transformation behavior during growth of nanocrystalline aggregates: insights from TiO_2 , *J. Phys. Chem. B* 104 (15) (2000) 3481–3487.
- [59] D.A.H. Hanaor, C.C. Sorrell, Review of the anatase to rutile phase transformation, *J. Mater. Sci.* 46 (2011) 855–874.
- [60] A. Fahmi, C. Minot, B. Silvi, M. Causa, Theoretical analysis of the structures of titanium dioxide crystals, *Phys. Rev.* 47 (18) (1993) 11717–11724.
- [61] V. Mauchamp, T. Épicier, J.-C. Le Bossé, Application of a fully relativistic theory to the EELS investigation of anisotropy effects at the oxygen K edge in rutile and ZrO_2 , *Phys. Rev. B* 77 (2008) 235122.
- [62] S.K. Misra, Multifrequency Electron Paramagnetic Resonance: Theory and Application, Wiley-VCN, Weinheim, Germany, 2011.
- [63] C. Di Valentin, K.M. Neyman, T. Risse, M. Sterrer, E. Fischbach, H.-J. Freund, V. A. Nasluzov, G. Pacchioni, N. Rösch, Density-functional model cluster studies of EPR g-tensors of F_5^{+} -centers on the surface of MgO , *J. Chem. Phys.* 124 (2006) 044708.
- [64] A. Abragam, B. Bleaney, *Electron Paramagnetic Resonance of Transition Ions*, Clarendon Press, Oxford (1970), p. 527–529.
- [65] S.K. Misra, S.I. Andronenko, K.M. Reddy, J. Hays, A. Thurber, A. Punnoose, A variable temperature Fe^{3+} electron paramagnetic resonance study of $Sn_{1-x}Fe_xO_2$ ($0.00 \leq x \leq 0.05$), *J. Appl. Phys.* 101 (2007) 09H120.
- [66] S.K. Misra, S.I. Andronenko, A. Punnoose, D. Tipikin, J.H. Freed, A 236-GHz Fe^{3+} EPR study of nano-particles of the ferromagnetic room-temperature semiconductor $Sn_{1-x}Fe_xO_2$ ($x=0.005$), *Appl. Magn. Res.* 36 (2-4) (2009) 291–295.
- [67] V.B. Kazanskiii, A.I. Mashchenko, Electron spin resonance investigation of radical form of molecular oxygen adsorption on reduced titanium dioxide, *Dokl. AN SSSR* 151 (2) (1963) 361–362.